

Development of superfluid helium-3 bolometry using nanowire resonators with SQUID readout for the QUEST-DMC experiment

QUEST-DMC Collaboration, E. Leason^{a,b*}, L. V. Levitin^b,
S. Autti^c, E. Bloomfield^a, A. Casey^b, N. Darvishi^b, N. Eng^b,
P. Franchini^a, R. P. Haley^c, P. J. Heikkinen^b, A. Jennings^d,
A. Kemp^e, J. March-Russell^a, A. Mayer^c, J. Monroe^a,
D. Münstermann^c, M. T. Noble^c, J. R. Prance^c, X. Rojas^b,
T. Salmon^c, J. Saunders^b, J. Smirnov^f, R. Smith^{a,b},
M. D. Thompson^c, A. Thomson^c, A. Ting^b, V. Tsepelin^c,
S. M. West^b, L. Whitehead^c, D. E. Zmeev^c

^a*Department of Physics, University of Oxford, Keble Road, Oxford, OX1 3RH, UK.*

^b*Department of Physics, Royal Holloway University of London, Egham, Surrey, TW20 0EX, UK.*

^c*Department of Physics, Lancaster University, Lancaster, LA1 4YB, UK.*

^d*RIKEN Center for Quantum Computing, RIKEN, Wako, 351-0198, Japan.*

^e*UKRI STFC Rutherford Appleton Laboratory, Particle Physics Department, Harwell, Didcot OX11 0QX, UK.*

^f*Department of Mathematical Sciences, University of Liverpool, Liverpool, L69 7ZL, UK.*

*Corresponding author(s). E-mail(s): elizabeth.leason@physics.ox.ac.uk;

Abstract

Superfluid helium-3 bolometers can be utilised for dark matter direct detection searches. The extremely low heat capacity of the B phase of the superfluid helium-3 at ultra-low temperatures offers the potential to reach world leading sensitivity to spin dependent interactions of dark matter in the sub-GeV/ c^2 mass range. Here, we describe the development of bolometry using both micron scale and

sub-micron diameter vibrating wire resonators, with a SQUID amplifier-based readout scheme. Characterisation of the resonators and bolometer measurements are shown, including the use of non-linear operation and the corresponding corrections. The bolometer contains two vibrating wire resonators, enabling heat injection calibration and simultaneous bolometer tracking measurements. Coincident events measured on both vibrating wire resonators verify their response. We also demonstrate proof of concept frequency multiplexed readout. Development of these measurement techniques lays the foundations for the use of superfluid helium-3 bolometers, instrumented with vibrating nano-mechanical resonators, for future low threshold dark matter searches.

1 Introduction

The QUEST-DMC programme uses a superfluid helium-3 bolometer for dark matter direct detection searches. This detection scheme, described in Ref. [1], is suited to sub-GeV/c² dark matter masses and has the potential to reach world leading sensitivity to dark matter interactions in this mass range [2, 3].

The bolometer exploits the extremely low heat capacity of the B phase of the superfluid helium-3 at ultra-low temperatures below 0.4 mK, where most quasiparticles are bound into Cooper pairs. Vibrating wire resonators are utilised primarily to measure the strongly temperature-dependent quasiparticle density and secondly as heaters for calibration. This technique was originally developed by the ULTIMA collaboration [4]. In QUEST-DMC we expect several orders of magnitude improvement in sensitivity as a result of two key developments: novel vibrating wire resonators with sub-micron diameter and Superconducting QUantum Interference Device (SQUID) readout.

We demonstrate the reliable SQUID readout of the bolometer with resonators in the non-linear regime close to the critical velocity. We show the use of a second vibrating wire as a heater, with much lower power heat injection than previously. Having two vibrating wires also allows for simultaneous tracking and coincident bolometer events are measured on both, verifying the response of the wires. The energy calibration with low-energy gamma rays and a study of noise performance of the bolometer will be subject of a separate report.

Our circuit contains no additional cryogenic components apart from the vibrating wire and integrated SQUID current sensor [5], in comparison to more complex schemes developed previously [6, 7]. This simplicity lends itself to scaling up by running an array of bolometers in parallel. Furthermore we demonstrate multiplexing by reading out two resonances with one SQUID simultaneously.

2 Experimental setup

The experimental assembly is illustrated in Fig. 1. A wet commercial dilution refrigerator was extended with a large copper nuclear demagnetisation stage. The bolometer is situated inside a mostly metallic cell filled with helium-3, mounted on top of the

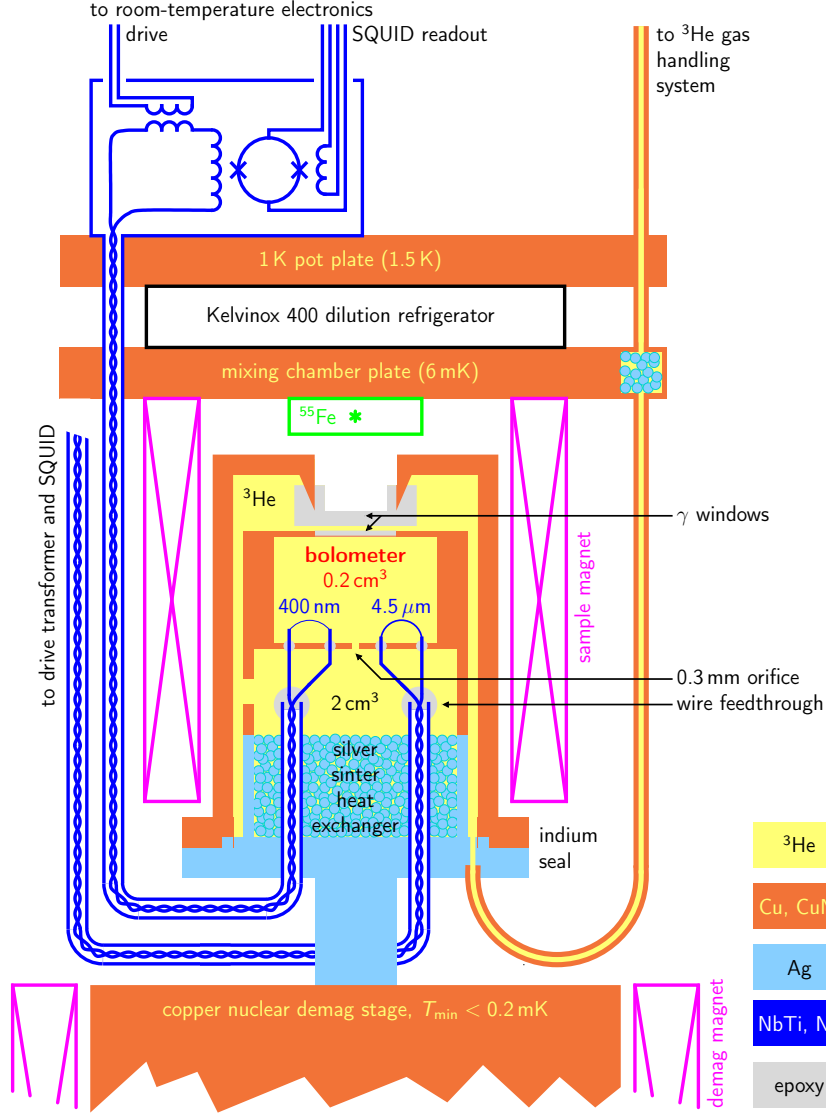


Fig. 1: Schematic drawing of the bolometer cell mounted on a nuclear demagnetisation refrigerator. The cell includes the silver sinter heat exchanger, reservoir of superfluid ^3He (2 cm^3) and bolometer opened to the reservoir via a small orifice. The base of the cell is in good thermal contact with the copper demagnetisation stage, precooled by an Oxford Instruments Kelvinox 400 dilution refrigerator (DR). The bolometer is equipped with thermometer/heater vibrating wires, connected to SQUID sensors with integrated drive transformers, mounted at the 1 K pot plate of DR. The magnetic fields for the operation of vibrating wires is provided by a small superconducting magnet, separate from the large demagnetisation magnet situated in the ^4He bath of the cryostat. The bolometer and cell walls include gamma ray transparent windows for energy calibration using a ^{55}Fe source located outside the cell.

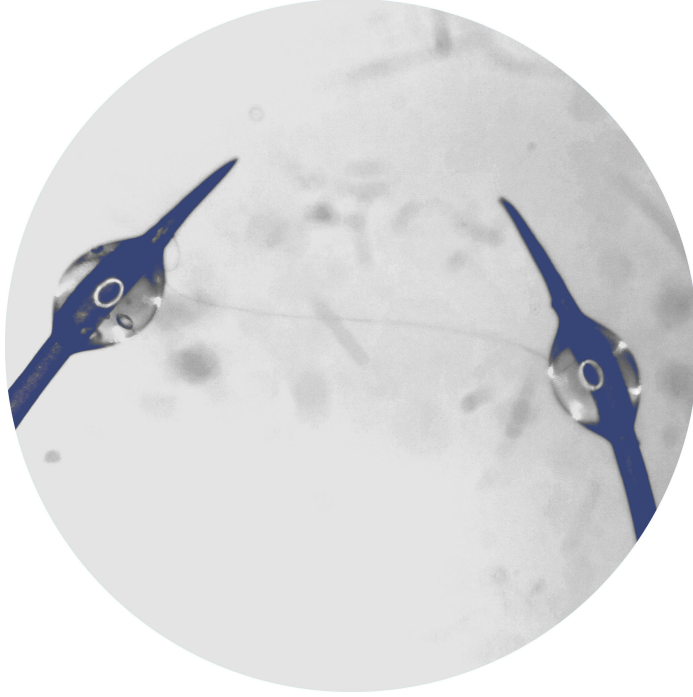


Fig. 2: A 400 nm nanowire photographed through an optical microscope. Araldite epoxy beads stabilises the extruded superconducting cable at both ends of the wire. In the section between the beads all filaments but one were removed after etching away the copper matrix.

demagnetisation stage. Helium-3 in the main reservoir of roughly 2 cm^3 is cooled by a silver sinter heat exchanger of estimated surface area 20 m^2 .

The superfluid helium-3 bolometer is a $7 \times 5 \times 5\text{ mm}$ cuboid open to the main reservoir via a 0.3 mm diameter orifice, which provides the cooling of the superfluid helium-3 target. A well-defined bolometer volume is essential to establishing a reliable energy calibration. To this end the bolometer cavity was machined out of a solid copper puck, with the upper and lower walls constructed from flat copper foils. This essentially metallic construction ensures no heating of the bolometer due to heat release in disordered materials such as paper and epoxies, traditionally used in construction of helium-3 bolometers. Minimal amounts of Stycast 1266 and Araldite epoxies were used to seal the joints between the puck and foils and for the vibrating wire feedthroughs. The main materials used have been screened in the Boulby Underground Germanium Screening facility to ensure acceptable levels of radiopurity [8].

The bolometer contains NbTi vibrating wires of two diameters: the 4500 nm wires were obtained commercially as filaments of a multifilament superconducting cable in copper matrix; the 400 nm nanowires, Fig. 2, were produced by drawing such cable through a series of dies, similar to the procedure described in Ref. [9]. Sections of

complete cable at both ends of the vibrating wires served as ‘legs’ and were mounted in the bolometer wall using Araldite epoxy.

The vibrating wires are connected to SQUID current sensors, installed on the 1 K pot plate of the dilution refrigerator. Transformers integrated into the SQUIDs were used to drive the vibrating wires [5]. The electrical connections to the cell are minimal: a single NbTi twisted pair shielded inside a Nb tube per vibrating wire. This electrical circuit and its performance are discussed in Sec. 3 below.

The magnetic field for electrical excitation and readout of the mechanical resonators is provided by a small superconducting magnet suspended off the mixing chamber plate of the dilution refrigerator. The nuclear stage is also rigidly attached to this plate, minimising relative motion of the bolometer and the magnet. In the earlier Lancaster-style design [1] the bolometer is embedded inside an assembly of sintered nuclear stages, to reach exceptionally low helium temperatures. In contrast, here we can alter the sample field independent of the demag field, in order to investigate the performance of the SQUID readout.

In addition to direct heat injection, our approach to energy calibration will use low energy deposition from a well-characterised ^{55}Fe source. The standard packaging of commercial radioactive sources is too bulky to incorporate these inside the cell, thus the cell and bolometer walls have windows with reduced gamma photon attenuation. Our ^{55}Fe source has a low nominal activity ensuring no prohibitive heat release in any part of the setup and making the handling of the source safe. The 1 mm thick Stycast 1266 epoxy window in the cell lid and 5 μm copper foil window in the bolometer were selected to have sufficient strength and appropriate gamma attenuation.

Important properties of the superfluid helium-3 target can be tuned with pressure [10], therefore we designed the cell capable to withstand tens of bars. The wire feedthroughs and the outer gamma window are positioned on the inside of the cell, so that the helium under pressure squeezes epoxy around metal tubes. The cell has been successfully leak tested up to 20 bar. While the pressure inside the bolometer is normally the same as in the main reservoir, transient pressure gradients are unavoidable when loading or emptying the cell. To prevent deformation or damage to the 5 μm copper window in the bolometer wall this was reinforced with a $\sim 100\text{ }\mu\text{m}$ film of Stycast 1266 with negligible gamma attenuation.

All measurements presented in this paper were obtained at a cell pressure of 18.5 bar, stabilised to 1 mbar using a quartz pressure transducer and a heated gas volume operated by a proportional-integral controller. At this pressure the superfluid transition is at $T_c = 2.2\text{ mK}$ and the lowest temperature reached in the bolometer was $0.135 T_c$.

3 SQUID readout scheme

The scheme for reading out the voltage-driven vibrating wire, using a 2-stage SQUID current sensor [5], is shown in Fig. 3. Voltage $V_x = 2i\pi f M_x I_x$ is applied inductively by driving the current I_x at frequency f , via the transformer with mutual inductance M_x . This current is generated by a voltage oscillator via a resistor $R_x = 1\text{--}100\text{ k}\Omega$. The SQUID detects the current I_i flowing through the loop comprised of the wire of

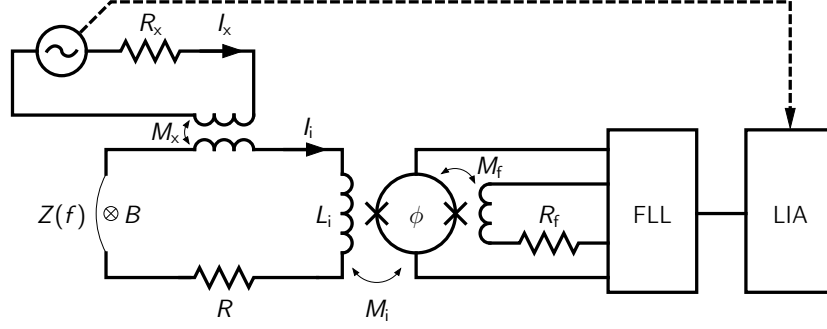


Fig. 3: SQUID readout circuit. The vibrating wire forms part of an input loop of a SQUID current sensor together with contact resistance R , input coil L_i of the SQUID and drive transformer with mutual inductance M_x . The wire is excited by voltage V_x , applied by driving a current, I_x , via the transformer with mutual inductance M_x . The SQUID operated in flux-locked loop (FLL) detects the current I_i in the loop. The FLL gain is determined by R_f and M_f . A phase-sensitive lock-in amplifier (LIA) detects the component of I_i at the frequency of the drive.

impedance Z , SQUID input coil of inductance L_i (including inductance of the twisted pair between the wire and the SQUID, and self-inductance of the secondary of the drive transformer) and series resistance R of the contacts/wire,

$$I_i = \frac{V_x}{Z_\Sigma} = \frac{V_x}{Z + R + 2i\pi f L_i}. \quad (1)$$

Here, $Z_\Sigma = Z + R + 2i\pi f L_i$ is the total impedance of the loop. This gives flux $\phi = M_i I_i$ in the SQUID, which is read out using flux-locked loop electronics [11]. Note that all alternating currents, voltages, forces, velocities and powers are rms throughout.

We infer I_i from the real and imaginary components, X and Y , of the voltage measured by the lock-in at the output of the flux-locked loop,

$$I_i = \frac{X + iY}{(R_f/M_f) \times M_i}. \quad (2)$$

Here, R_f is resistance of the feedback resistor, M_f is the mutual inductance between the feedback coil and the SQUID, M_i is the mutual inductance between the input coil and the SQUID. This is used to calculate the impedance of the wire,

$$Z = \frac{2i\pi f M_x}{I_i/I_x} - R - 2i\pi f L_i. \quad (3)$$

3.1 Broad frequency sweeps

The propagation of the signal through the measurement circuit leads to a correction, that we model by,

$$I_i \rightarrow \left(1 - \frac{if_c}{f}\right) \exp(-ia - ibf) I_i. \quad (4)$$

Here, the first term describes the AC input coupling of the lockin, which acts as a first-order high pass filter with cutoff frequency $f_c = 80$ Hz. The second term represents the rest of the circuit, where a simple phenomenological expression $a + bf$ for the phase shift proves adequate. This correction is applied to the measured I_i prior to evaluation of the impedance according to Eq. (3).

The values of a and b as well as circuit parameters R and L_i are obtained from broad (5 Hz–10 kHz) frequency sweeps carried out at zero magnetic field, where there is no contribution to the total impedance of the SQUID input loop from the vibrating wire resonators, and the data can be fitted to Eq. (3) with $Z = 0$.

4 Resonator characterisation

4.1 Narrow frequency sweeps

In order to characterise the vibrating wire resonances narrow frequency sweeps were carried out at constant I_x in a range of magnetic fields, illustrated by Fig. 4. The impedance obtained from Eq. (3) was fitted to a Lorentzian,

$$Z(f) = \frac{ifA}{f_0^2 - f^2 + ifdf}, \quad (5)$$

with resonance amplitude A and resonance frequency f_0 . The resonance width df includes contributions from both the intrinsic (as observed in vacuum) and quasiparticle damping. The latter is a direct measure of the bolometer temperature, enabling the tracking measurements described in Section 5.

In the simple approximation of a rigid beam moving rectilinearly perpendicular to the magnetic field the resonance amplitude $A = \ell B^2 / 2\pi m$ can be parametrised by effective length ℓ and mass per unit length m of the vibrating wire [7]. We find $\ell = 1.0$ mm for the 1.4 mm-long 400 nm nanowire and $\ell = 0.9$ mm for the 1.9 mm-long 4500 nm wire. The discrepancy between ℓ and the actual wire length, more pronounced for the arched 4500 nm wire, arises from the distribution of velocity and displacement along the wire. Extracting ℓ from A enables us to estimate the velocity,

$$v = \frac{|V|}{\ell B} = \frac{|ZI_i|}{\ell B}, \quad (6)$$

from the voltage V across the wire, also shown in Fig. 4. Note that the raw data $I_i(f)/I_x$ look drastically different for the two wires at the same field and temperature, representing the cases of $Z(f_0) \gg \omega L_i$ and $Z(f_0) < \omega L_i$ for the 400 nm and 4500 nm wires respectively.

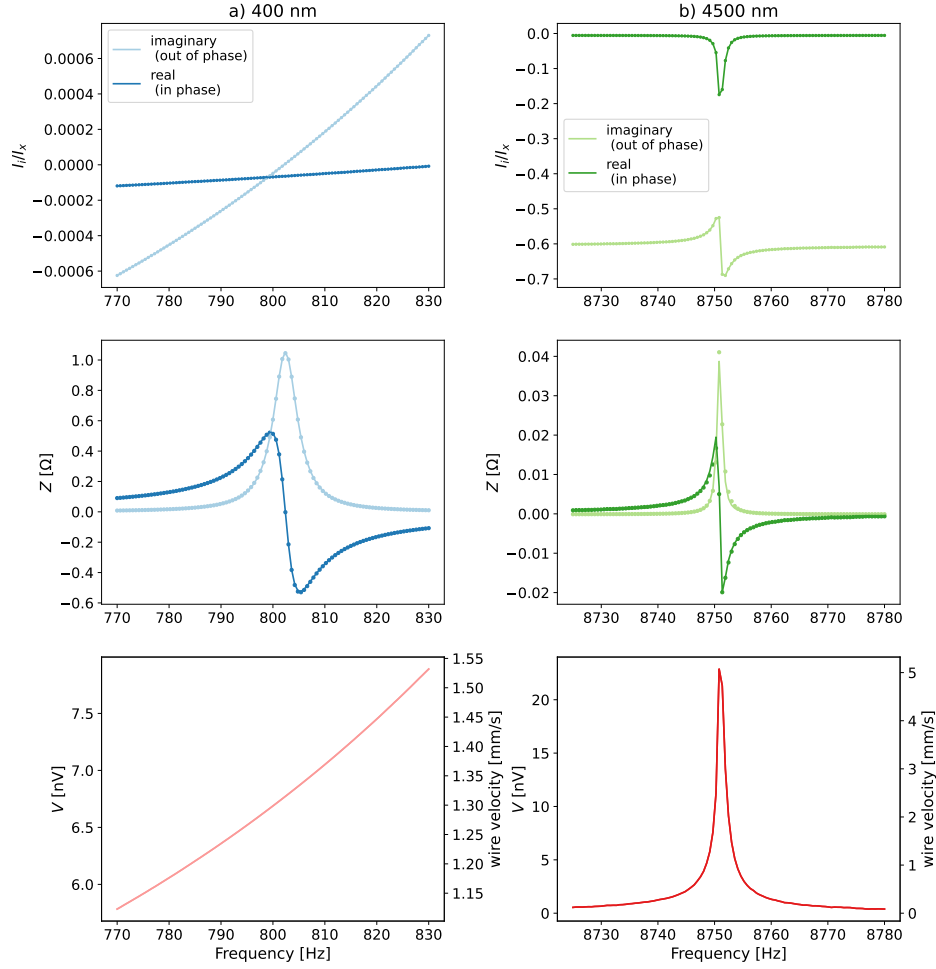


Fig. 4: Frequency sweeps for the a) 400 nm nanowire and b) 4500 nm wire – both at 18.5 bar, 0.27 mK and 5.2 mT field. The top panel shows the ratio of measured current to drive current and resonance-like behaviour depends on the relationship between them. The middle panel shows the impedance of the wire. The lower panel shows the derived voltage across the wire and root mean squared velocity of the wire.

4.2 Drive amplitude sweeps

The drive amplitude and therefore velocity dependence of the wire response can be characterised with drive amplitude sweeps at a fixed frequency, typically on resonance. To a geometrical factor of order unity, we estimate the force on the wire as,

$$F = |I_i \ell B|. \quad (7)$$

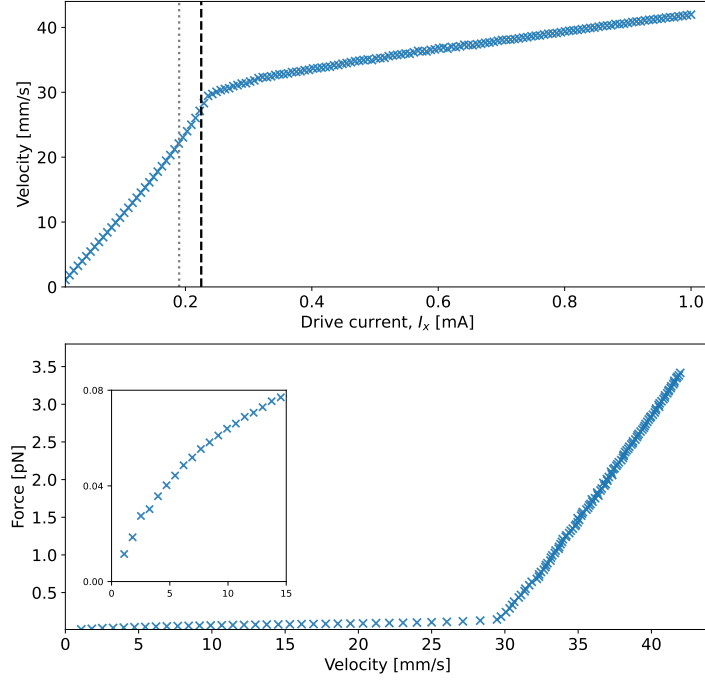


Fig. 5: Drive amplitude sweep for the 400 nm nanowire at the resonant frequency of 799 Hz. Upper plot shows rms velocity vs drive current, with dotted grey and dashed black lines indicating the selected tracking drive and critical velocity, respectively. Lower plot shows the corresponding drive force vs velocity, demonstrating characteristic regions of quasiparticle injection and non-linearity.

On-resonance drive sweeps on 400 nm nanowire are shown in Fig. 5. When oscillating at small velocities the response of the wire is linear, with a linear damping force $F_d \propto v$. However, as velocity increases beyond a few mm/s the damping becomes nonlinear, this change around $k_B T / p_F \simeq 4$ mm/s, consistent with expectation [12].

As velocity is increased further, emission of bound quasiparticles into the bulk superfluid leads to an increase in dissipation [13, 14], giving a sharp rise in $F_d(v)$ observed at $v = 32$ mm/s, of order Landau critical velocity $v_L = \Delta / p_F \simeq 60$ mm/s. For a macroscopic wire of circular cross-section with diameter much greater than the coherence length $\xi_0 = 22$ nm (at 18.5 bar), this phenomenon is predicted to onset at rms velocity $v_L / 3\sqrt{2} = 14$ mm/sec. Here, the discrepancy may reflect neglecting the velocity distribution along the wire in Eq. (6) and/or the mesoscopic character ($d \sim 10 \xi_0$) of the 400 nm nanowire.

4.3 Non-linearity correction

Whilst below critical velocity, the operating velocity is beyond the linear regime. The non-linearity manifests via a velocity-dependent resonance width $df(v)$ and can be taken into account following Ref. [15]. From Eq. (5) this width can be obtained as,

$$df(v) = \text{Re}\left(\frac{A}{Z(f, v)}\right), \quad (8)$$

from a single impedance measurement $Z(f, v)$ at a frequency f and velocity v . The resonance amplitude A is determined by fitting Eq. (5) to a low-drive frequency sweep, typically at sub mm/s velocity. In principle Eq. (8) is valid at any measurement frequency, but practically the high-resolution determination of $df(v)$ is limited to the vicinity of the resonance where Z is predominantly real.

The measured width can be written as the sum of intrinsic and quasiparticle damping terms,

$$df(v) = df_i + df_0 S(\gamma v / v_0). \quad (9)$$

Here, the intrinsic damping is characterised by the width $df_i = 0.15$ Hz measured for both resonators in vacuum prior to filling the cell with helium-3. The second term is

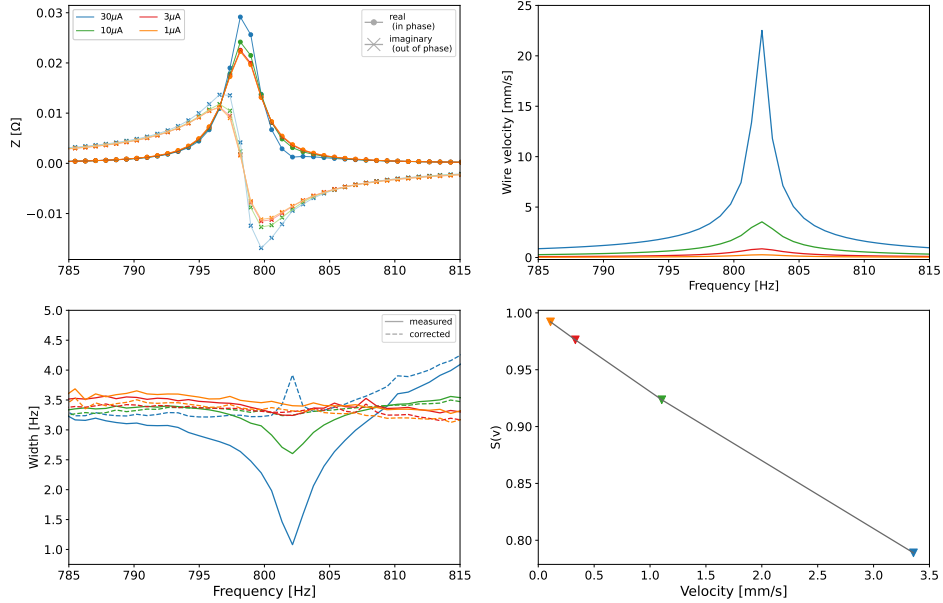


Fig. 6: Demonstration of the non-linearity correction for the 400 nm nanowire. Upper left: frequency sweeps at different drives. Upper right: corresponding velocity across the sweep. Lower left: width inferred from Eq. (8) before and after correction to the linear regime using Eq. (9). Lower right: correction factor $S(v)$ as a function of velocity, the triangles represent the correction applied on resonance.

the width due to quasiparticle damping only. Following Ref. [15] we express it as a product of the width df_0 at $v \rightarrow 0$ and a correction factor,

$$S(c) = \frac{2}{c} \left(I_1(c) - L_{-1}(c) + \frac{2}{\pi} \right), \quad (10)$$

determined by the reduced velocity $c = \gamma v/v_0$. Here, γ is a dimensionless adjustable parameter of order unity that encodes the velocity profile, I_1 is the modified Bessel function of the first kind of real order 1 and L_{-1} is the modified Struve function of order -1 . Thus we extract $df_0 = (df(v) - df_i)/S(\gamma v/v_0)$ simplifying further analysis of the bolometer response. The performance of this correction procedure up to velocities of tens of mm/s is illustrated in Fig. 6. Here we note again that the 400 nm oscillator is mesoscopic ($R \gg \xi_0$ does not hold), therefore departures from Eqs. (9, 10) are expected [16]. To improve the non-linearity correction the distribution of velocity along the wire can be considered, this will be the subject of future work.

5 Bolometer measurements

To operate the cell as a bolometer the resonator is interrogated at the resonant frequency and a constant drive level, below the onset of pair breaking and low enough for the non-linearity correction to work, see Sections 4.2, 4.3. From the measured wire impedance Z we obtain the resonance width df_0 (corrected for finite velocity and intrinsic damping) according to Eqs. (8)-(10). This procedure takes the resonance amplitude A as an input parameter, so the tracking is stopped several times a day for low-drive frequency sweeps.

Figure 7 illustrates tracking measurements. The bolometer response to a heating event at time t_{peak} can be described as a function of time,

$$df_0(t) = df_0^{\text{base}} + \Theta(t - t_{\text{peak}}) H_{\text{peak}} \left[\left(\frac{\tau_b}{\tau_w} \right)^{\tau/(\tau_b - \tau_w)} \times \frac{\tau_b}{\tau_b - \tau_w} (e^{-t/\tau_b} - e^{-t/\tau_w}) \right], \quad (11)$$

where df_0^{base} is the baseline width, H_{peak} is the peak amplitude and $\Theta(t)$ is the Heaviside step function. The two time constants, which determine the pulse shape, are: the bolometer time constant τ_b and the wire time constant τ_w . These four parameters are determined by fitting found pulses in the tracking mode data. The amplitude H_{peak} depends on the magnitude of heating (or energy) causing the event. The other three parameters should remain constant for a given dataset: df_0^{base} depends on bolometer temperature, τ_w is a temperature dependent wire property and τ_b depends on the bolometer geometry.

Most of the instantaneous heating events in the bolometer result from particles such as cosmic rays or radioactive decay products interacting with the superfluid helium [1, 8]. An example bolometer pulse is shown in Fig. 7 and large pulses such as this one most likely originate from cosmic ray interactions.

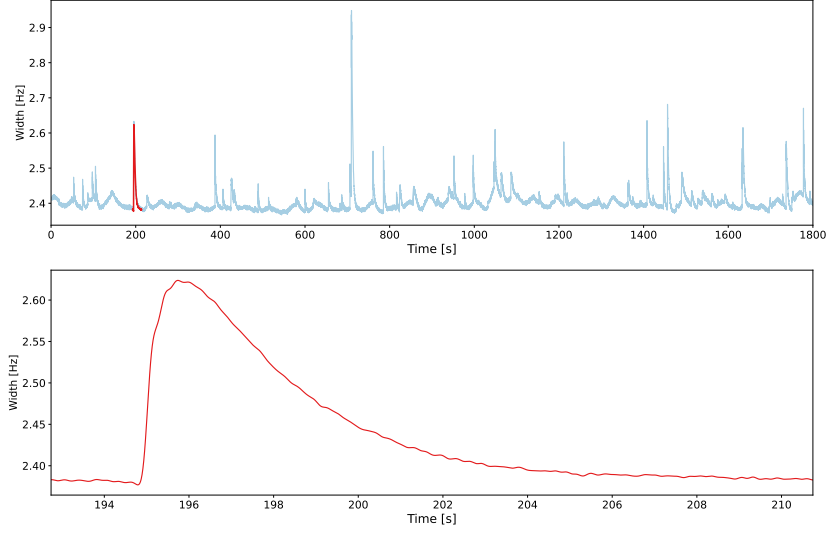


Fig. 7: Example tracking data from 400 nm nanowire, driven on resonance in a 5.2 mT field at 0.3 mK. Example bolometer pulse shape shown in the lower panel.

6 Two-wires operation

6.1 Heat injection calibration

The bolometric technique relies on conversion of the resonance width change, observed in the tracking measurements, to temperature change or energy. Width of the resonance is proportional to the damping force, F_d , from momentum transfer in quasiparticle collisions with the wire [17],

$$df_0 = \alpha \frac{F_d}{2\pi m v} = \gamma' \frac{dp_F^2 \langle n v_g \rangle}{2\pi m k_B T} = \gamma' \frac{8dp_F^4}{mh^3} \exp(-\Delta/k_B T). \quad (12)$$

Here, d is the wire diameter, p_F is the Fermi momentum, $\langle n v_g \rangle$ is the density of quasiparticle or quasihole excitations n multiplied by the appropriate group velocity v_g and Δ is the superfluid gap at the operating temperature and pressure. Dimensionless constants α and γ' depend on wire geometry and details of the scattering process. This enables conversion of measured widths to temperature and energy, once bolometer calibration has determined the value of γ' . One calibration method, demonstrated in Refs. [4, 17, 18], is to use to inject heat into the system by mechanical dissipation.

For heat injection over time scales longer than the bolometer time constant the bolometer will reach thermal equilibrium as a result of quasiparticle-wall and

quasiparticle-quasiparticle collisions. This means the number density of quasiparticles will quickly become constant and frequency width reaches a new stable value. In this state the total power entering the bolometer, from both the heater and wall heat leaks, must balance power carried by the quasiparticles leaving the orifice, $\dot{Q}_T = \dot{Q}_h + \dot{Q}_w = \dot{Q}_o$. The power transmitted out through the orifice can be written as [17],

$$\dot{Q}_o = \frac{\langle nv_g \rangle}{4} \langle E \rangle A_o. \quad (13)$$

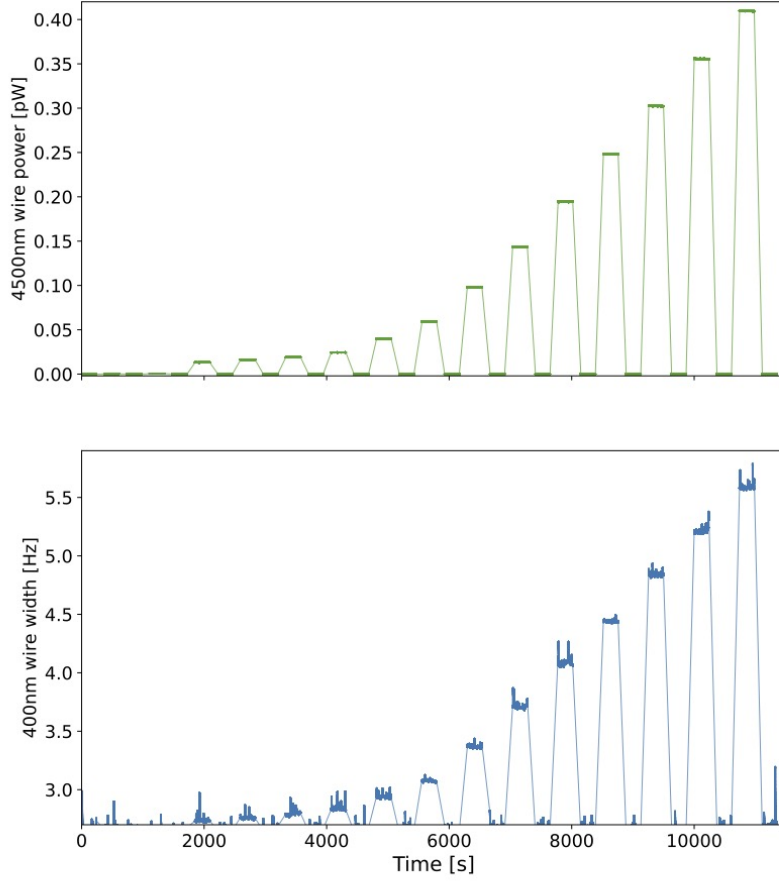


Fig. 8: Stepped heat injection using the 4500 nm wire driven above critical velocity (upper) and the measured width response of the 400 nm nanowire (lower).

Here, $\langle E \rangle$ is the average quasiparticle energy and A_o is the effective area of the orifice. This can be determined from the bolometer time constant $\tau_b = 4V_b/A_o\langle v_g \rangle$ for bolometer volume V_b and mean quasiparticle group velocity $\langle v_g \rangle \approx \sqrt{k_B T / \Delta v_F}$. Combining with Eq. (12) the width can be related to total power,

$$df_0 T \langle E \rangle = \gamma' \frac{2dp_F^2}{\pi k_B m A_o} \dot{Q}_T. \quad (14)$$

Subtracting input power from the walls using the bolometer base width, df_0^{base} , and substituting $\langle E \rangle = \Delta + k_B T$ allows us to define the width parameter [18],

$$W_p = (df_0 - df_0^{\text{base}}) T \left(\frac{\Delta}{k_B} + T \right). \quad (15)$$

This absorbs the temperature dependence of $\langle E \rangle$ in Eq. (14) such that the bolometer response can be related to applied heater power,

$$W_p = \gamma' \frac{2dp_F^2}{\pi k_B m A_o} \dot{Q}_h. \quad (16)$$

The calibration constant γ' can be determined from the steady-state response $df_0(\dot{Q}_h)$, as shown in Fig. 8. Periods of zero applied power were inserted between each period of constant heating, in order to correct for any temporal variations in d_0^{base} . The 4 minute wait at each power, much longer than τ_b , ensures the equilibrium. Even though the 4500 nm wire as a heater operates in a non-linear regime, the detected current $I_i(t)$

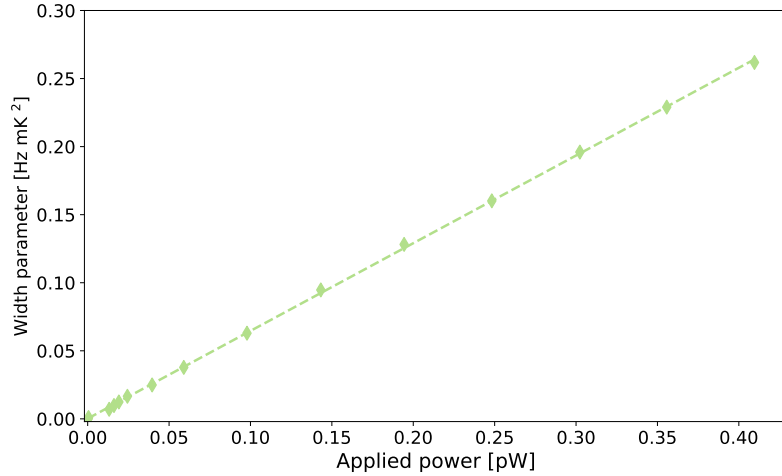


Fig. 9: Linear relationship between power injected by the 4500 nm wire and width parameter measured using the 400 nm nanowire.

in time-domain is nearly sinusoidal. Therefore we derive the power applied using the wire as $\dot{Q}_h = |I_i|^2 \text{Re}(Z)$.

Figure 9 shows the linear response of the measured width parameter on the 400 nm nanowire, defined in Eq. (15), to injected power. This validates our model and assumption of thermal equilibrium in the bolometer. The linear fit was consistent for different 400 nm drive amplitudes and tracking measurements times. Once the calibration constant has been extracted from this fit, Eq. (12) can be used to find energy of individual pulse events using either the measured pulse amplitude or area.

6.2 Simultaneous tracking

Tracking data was acquired on both wires simultaneously, at 2.6 mT field and 0.3 mK bolometer temperature. Since the bolometer slowly warms up after a demagnetisation the tracking measurements were periodically paused for i) low-drive frequency sweeps to recalibrate resonance amplitude A and ii) heater calibrations.

In this dataset simultaneous heating events can be observed on the two wires. Figure 10 shows an example of simultaneous pulses, fit with the expected bolometer heating pulse shape from Eq. (11). Here, higher baseline noise is seen in the 4500 nm tracking data due to the lower field. The pulse shape fits for this dataset show consistent bolometer time constant of 3 s for both wires and rise times of 0.2 s and 0.6 s for the 400 nm and 4500 nm wire respectively. There was a factor of 10 difference observed in the width change for the two wires. This is roughly consistent with the ratio of the wire diameters, however may not be exact due to mesoscopic character of the thinner wire.

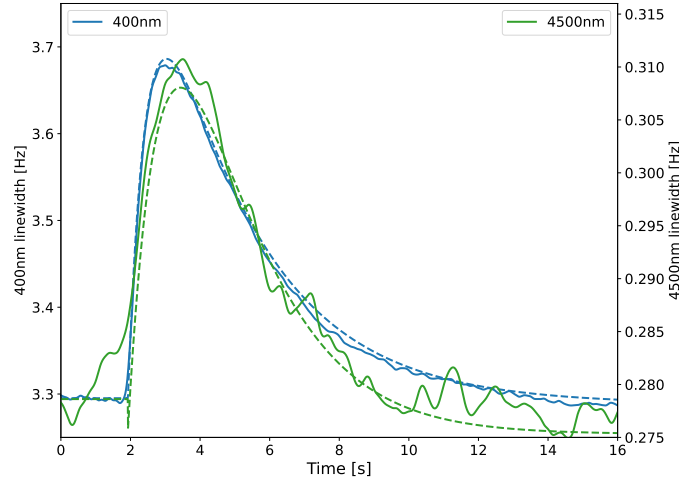


Fig. 10: Coincident bolometer pulses observed when tracking on both wires simultaneously, solid line shows data and dashed line shows the fit to Eq. (11).

6.3 Multiplexing

Figure 11(a) shows how several vibrating wires can be simultaneously read out by a single SQUID sensor. Provided the resonances are sufficiently separated in frequency, the wires make negligible contributions to the total impedance of the input loop near

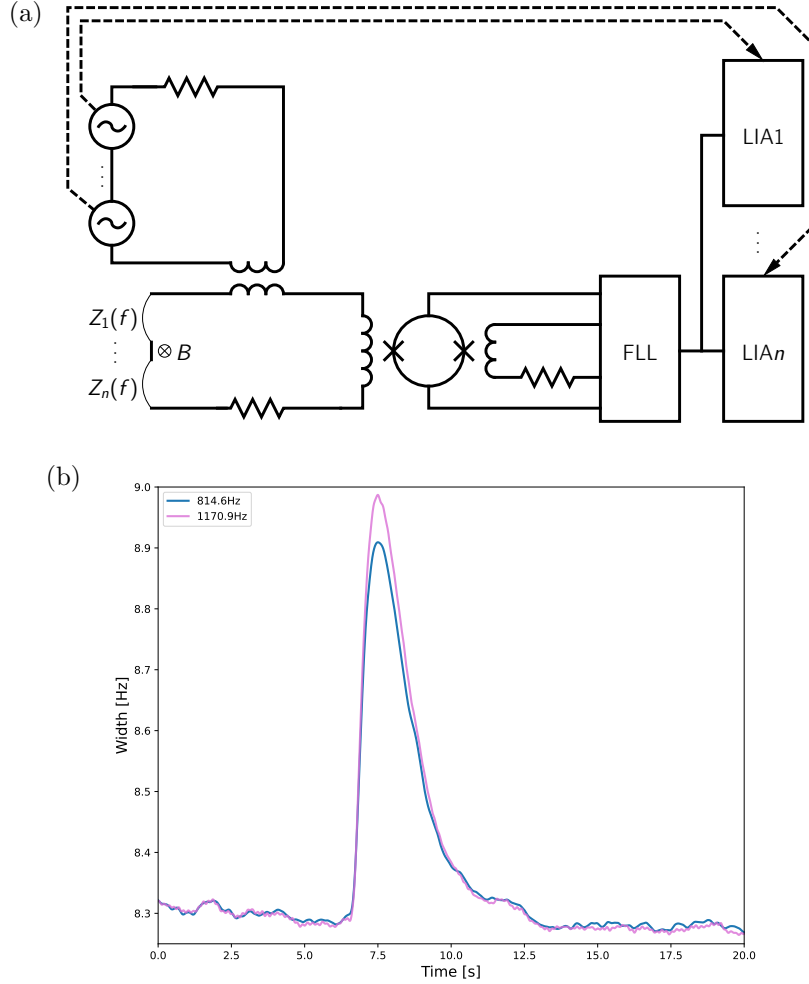


Fig. 11: Readout of multiple vibrating wires with one SQUID sensor. (a) Circuit diagram. All vibrating wires represented by the impedances $Z_1(f)$, \dots , $Z_n(f)$ must resonate at sufficiently different frequencies. A single state-of-the-art multichannel lock-in amplifier is capable of driving and detecting multiple resonances simultaneously. (b) Simultaneous tracking measurements on two vibrations modes of the same 400 nm nanowire as a proof of principle.

each other’s resonance. Moreover, off-resonance drive generates no discernible motion in the wires, allowing to drive simultaneously all wires close to the critical velocity. Here, we demonstrate this concept, in a different bolometer, using a 400 nm nanowire, that exhibits an additional low-frequency vibrational mode due to fabrication/mounting issues. The simultaneous readout of the two vibrational modes with a single SQUID is illustrated in Fig. 11(b).

7 Conclusions and outlook

We have demonstrated the operation of a superfluid helium-3 bolometer at sub-millikelvin temperatures, using nanomechanical resonators with SQUID read out. Using a second wire for calibration in this scheme allows for injection of much lower heat power than has been done previously, reaching the energy region of interest for a low mass particle dark matter search.

This lays the foundation for detection of energy deposits from particle interactions in the superfluid. The next development will be a comparison of energy deposits from particle calibration sources with the energy injection using a heater wire, together with characterisation and optimisation of the energy resolution. This will inform the energy partition model used in the dark matter search analysis outlined in Ref. [1]. Further studies will also include detailed understanding of the noise performance and resonator geometry including the correspondence between these. The resonator design will be optimised for bolometer sensitivity, with the aim of minimising energy threshold achieved in the detector. Ultimately the resonator characterisation, bolometer calibration and tracking measurements described here will be optimised for a dark matter search and utilised to perform this over a long exposure.

Acknowledgements

We thank Paul Bamford, Richard Elsom, Ian Higgs and Harpal Sandhu for excellent technical support.

Funding. This work was funded by UKRI EPSRC and STFC (Grants ST/T006773/1, ST/Y004434/1, EP/P024203/1, EP/W015730/1 and EP/W028417/1), as well as the European Union’s Horizon 2020 Research and Innovation Programme under Grant Agreement no 824109 (European Microkelvin Platform). S.A. acknowledges financial support from the Jenny and Antti Wihuri Foundation. M.D.T acknowledges financial support from the Royal Academy of Engineering (RF/201819/18/2). J.Sm. acknowledges support from the UK Research and Innovation Future Leader Fellowship MR/Y018656/1. A.K. acknowledges support from the UK Research and Innovation Future Leader Fellowship MR/Y019032/1.

References

- [1] Autti, S. *et al.* QUEST-DMC superfluid helium-3 detector for sub-GeV dark matter. *The European Physical Journal C* **84** (2024). URL <http://dx.doi.org/10.1140/epjc/s10052-024-12410-8>.

- [2] Darvishi, N. *et al.* Dark matter attenuation effects: sensitivity ceilings for spin-dependent and spin-independent interactions. *J. Cosm. Astropart. Phys.* **2025**, 017 (2025). URL <http://dx.doi.org/10.1088/1475-7516/2025/04/017>.
- [3] Darvishi, N. *et al.* Dark matter eft landscape probed by quest-dmc (2025). URL <https://arxiv.org/abs/2505.17995>. 2505.17995.
- [4] Winkelmann, C. *et al.* Bolometric calibration of a superfluid ^3He detector for dark matter search: Direct measurement of the scintillated energy fraction for neutron, electron and muon events. *Nucl. Instrum. Methods Phys. Res. A.* **574**, 264–271 (2007). URL <http://dx.doi.org/10.1016/j.nima.2007.01.180>.
- [5] Drung, D. *et al.* Highly sensitive and easy-to-use SQUID sensors. *IEEE Trans. Appl. Supercond.* **17**, 699–704 (2007).
- [6] Bradley, D. I. & Hayes, W. M. An rf-squid amplifier system for use with vibrating wire resonators. *J. Low Temp. Phys.* **119**, 703–713 (2000). URL <https://doi.org/10.1023/A:1004689830846>.
- [7] Martikainen, J. & Tuoriniemi, J. T. SQUID amplifier system for vibrating wire resonators. *J. Low Temp. Phys.* **124**, 367–382 (2001). URL <https://doi.org/10.1023/A:1017554708219>.
- [8] Leason, E. *et al.* QUEST-DMC: Background modelling and resulting heat deposit for a superfluid helium-3 bolometer. *J. Low Temp. Phys.* **215**, 465–476 (2024). URL <http://dx.doi.org/10.1007/s10909-024-03142-w>.
- [9] Autti, S. *et al.* Long nanomechanical resonators with circular cross-section (2023). URL <https://arxiv.org/abs/2311.02452>. arXiv:2311.02452.
- [10] Vollhardt, D. & Wölfle, P. *The superfluid phases of helium 3* (Dover Publications, New York, 2013), Dover edn.
- [11] Drung, D., Hinnrichs, C. & Barthelmess, H. Low-noise ultra-high-speed dc SQUID readout electronics. *Supercond. Sci. Technol.* **19**, S235–S241 (2006).
- [12] Fisher, S. N., Guénault, A. M., Kennedy, C. J. & Pickett, G. R. Beyond the two-fluid model: Transition from linear behavior to a velocity-independent force on a moving object in $^3\text{He-B}$. *Phys. Rev. Lett.* **63**, 2566–2569 (1989). URL <https://link.aps.org/doi/10.1103/PhysRevLett.63.2566>.
- [13] Autti, S. *et al.* Fundamental dissipation due to bound fermions in the zero-temperature limit. *Nat. Commun.* **11** (2020). URL <http://dx.doi.org/10.1038/s41467-020-18499-1>.
- [14] Autti, S. *et al.* Transport of bound quasiparticle states in a two-dimensional boundary superfluid. *Nat. Commun.* **14** (2023). URL <http://dx.doi.org/10.1038/>

s41467-023-42520-y.

- [15] Zavjalov, V. V. Using vibrating wire in non-linear regime as a thermometer in superfluid $^3\text{He-B}$ (2023). URL <https://arxiv.org/abs/2303.01189>. arXiv:2303.01189.
- [16] Autti, S. *et al.* Drag on cylinders moving in superfluid $^3\text{He-B}$ as the dimension spans the coherence length. *J. Low Temp. Phys.* **217**, 264–278 (2024). URL <http://dx.doi.org/10.1007/s10909-024-03165-3>.
- [17] Bäuerle, C., Bunkov, Y. M., Fisher, S. N. & Godfrin, H. Temperature scale and heat capacity of superfluid $^3\text{He-B}$ in the $100\mu\text{K}$ range. *Phys. Rev. B* **57**, 14381–14386 (1998). URL <https://link.aps.org/doi/10.1103/PhysRevB.57.14381>.
- [18] Fisher, S. N., Guénault, A. M., Kennedy, C. J. & Pickett, G. R. Blackbody source and detector of ballistic quasiparticles in $^3\text{He-B}$: Emission angle from a wire moving at supercritical velocity. *Phys. Rev. Lett.* **69**, 1073–1076 (1992). URL <https://link.aps.org/doi/10.1103/PhysRevLett.69.1073>.